Journal Pre-proof

Fabrication and characterization of luminescent Pr^{3+} doped fluorapatite nanocrystals as bioimaging contrast agents

Dušan V. Milojkov, Oscar F. Silvestre, Vojislav Dj Stanić, Goran V. Janjić, Dragosav R. Mutavdžić, Marija Milanović, Jana B. Nieder

PII: S0022-2313(19)31123-8

DOI: https://doi.org/10.1016/j.jlumin.2019.116757

Reference: LUMIN 116757

To appear in: *Journal of Luminescence*

Received Date: 6 June 2019

Revised Date: 30 August 2019

Accepted Date: 18 September 2019

Please cite this article as: Duš.V. Milojkov, O.F. Silvestre, V.D. Stanić, G.V. Janjić, D.R. Mutavdžić, M. Milanović, J.B. Nieder, Fabrication and characterization of luminescent Pr^{3+} doped fluorapatite nanocrystals as bioimaging contrast agents, *Journal of Luminescence* (2019), doi: https://doi.org/10.1016/j.jlumin.2019.116757.

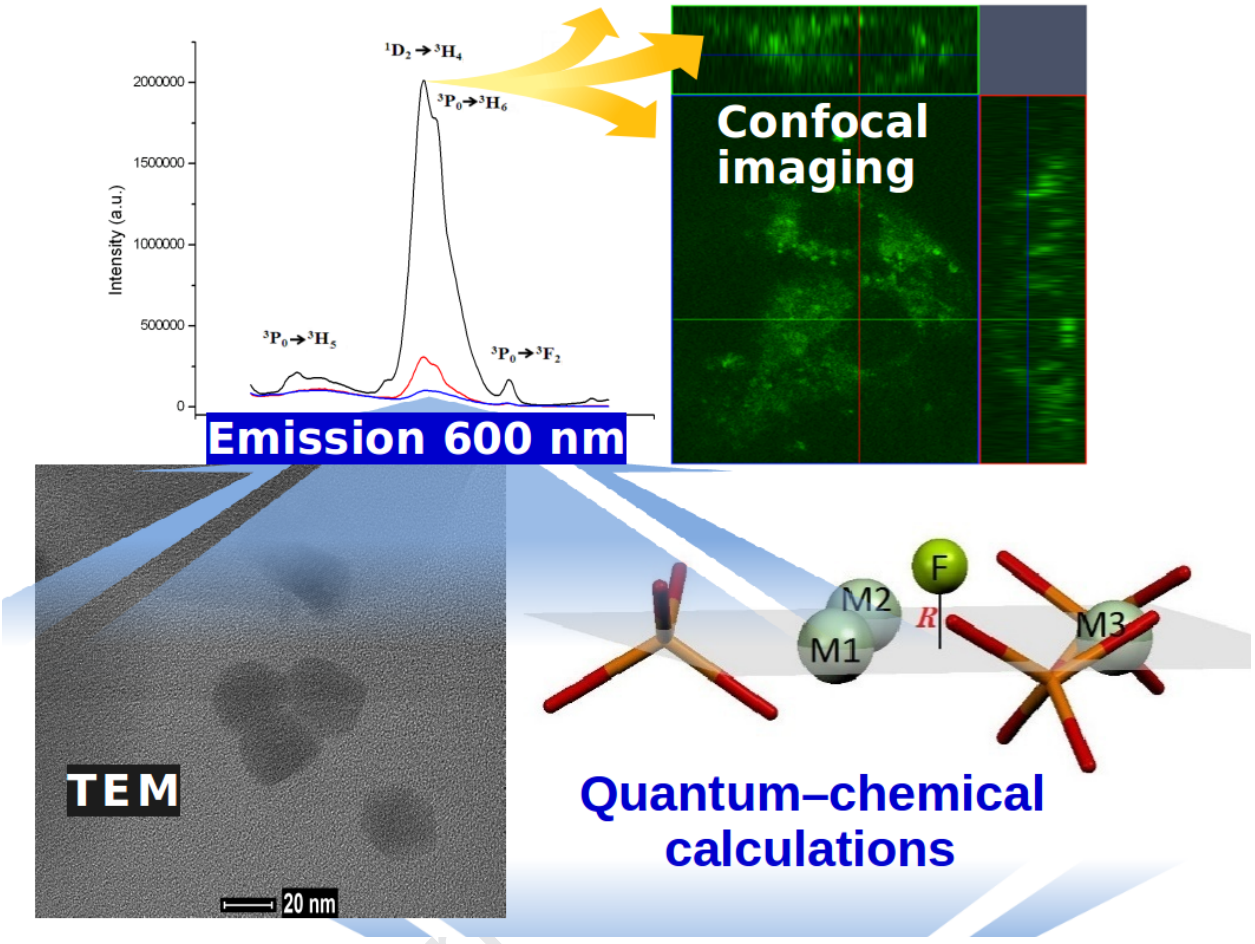
Intensity (a.u.)
2000000
1500000
1000000
500000
0
$^1D_2 \rightarrow {}^3H_4$
$^3P_0 \rightarrow {}^3H_6$
$^3P_0 \rightarrow {}^3H_5$
$^3P_0 \rightarrow {}^3F_2$
Emission 600 nm
Confocal imaging
TEM
20 nm
F
M2
M1
R
M3
Quantum–chemical calculations

Fabrication and characterization of luminescent Pr^{3+} doped fluorapatite nanocrystals as bioimaging contrast agents

Dušan V. Milojkov[a,b*], Oscar F. Silvestre[c], Vojislav Dj. Stanić[b], Goran V. Janjić[d], Dragosav R. Mutavdžić[e], Marija Milanović[a], Jana B. Nieder[c*]

[a] Department of Materials Engineering, Faculty of Technology Novi Sad, University of Novi Sad, Bulevar Cara Lazara 1, 21000 Novi Sad, Serbia

[b] Department of Radiation and Environmental Protection, Vinča Institute of Nuclear Sciences, University of Belgrade, P. O. Box 522, 11001 Belgrade, Serbia

[c] Department of Nanophotonics, Ultrafast Bio- and Nanophotonics Group, INL-International Iberian Nanotechnology Laboratory, Av. Jose Mestre Veiga, 4715-330 Braga, Portugal

[d] Department of Chemistry, Institute of Chemistry, Technology and Metallurgy, University of Belgrade, Studentski trg 12-16, 11000 Belgrade, Serbia

[e] Department of Life Sciences, Institute for Multidisciplinary Research, University of Belgrade, Kneza Višeslava 1, 11030 Belgrade, Serbia

*** Corresponding Authors:**

Jana B. Nieder, e–mail: jana.nieder@inl.int

Dušan V. Milojkov, e–mail: d.v.milojkov@gmail.com

Abstract

Fluorapatite doped with rare-earth elements has a wide-range of biomedical applications. Here, a new type of fluorapatite nanocrystals doped with praseodymium (FAP-Pr) with excitation-emission profiles in visible part of the spectrum is fabricated. Energy levels of Pr^{3+} activator ion contain metastable multiplet states that offer the possibility of efficient multicolor emission lines in FAP nanocrystals. Three types of FAP-Pr nanocrystals with 0.1%, 0.5% and 1% atomic percent of Pr^{3+} (along with the undoped FAP control sample) are studied. Their novel chemical production method is described, the FAP-Pr nanocrystals structure, biocompatibility and the suitability for cell imaging are analyzed. Physicochemical characterization confirms crystals down to nanometer size. In addition, quantum-chemical calculation predicts that Pr^{3+} ions are incorporated into the FAP crystal lattice at Ca2 (6h) sites. In vitro viability results shows that FAP-Pr nanocrystals are nontoxic to live cells. Additionally, the cell uptake of the FAP-Pr nanocrystals is studied using fluorescence-based widefield and confocal microscopy. The nanocrystals show characteristic green emission at 545 nm ($^3P_0 \rightarrow {}^3H_5$ transition of Pr^{3+} ion) and orange emission at 600 nm ($^1D_2 \rightarrow {}^3H_4$), which we use to discriminate from cell autofluorescence background. Orthogonal projections across 3D confocal stacks show that the nanocrystals are able to enter the cells positioning themselves within the cytoplasm. Overall, the new FAP-Pr nanocrystals are biocompatible and of the tested types, the 0.5% Pr^{3+} doped nanocrystals show the highest promise as a tracking nanoparticle probe for bioimaging applications.

Keywords: fluorapatite nanocrystals; praseodymium; bioimaging; cancer cells.

1. Introduction

Fluorapatite [($Ca_{10}(PO_4)_5F_2$), (FAP)] nanocrystals doped with rare-earth elements are ideal contrast agents for a variety of biomedical applications, e.g. detection, imaging, cell tracking, and therapy [1-4]. In FAP matrix F^- ions may lead to the formation of stable and biocompatible luminescent material with low vibrational energies, as well as phonon energies [1, 2]. These suitable energy profiles in FAP host matrix favour the rare-earth fluorescent transitions including those in up conversion and down-conversion luminescence. Compared to organic luminophores and semiconductors these nanocrystals have advantages such as photostability, a sharp visible emission bandwidth and nontoxicity [1-4]. The highest electronegativity of F^- ions in the FAP crystal lattice also contributes to their biocompatibility and complex tissue-nanomaterial interactions, which is important for long-term bioimaging studies [5, 6]. Additionally, the surface of FAP nanoparticles can be functionalized with a variety of groups and can become useful for the treatment of many diseases, such as clinical treatment for musculoskeletal system diseases, or cancer and neurodegenerative diseases [7-9].

So far, FAP has been used already quite often as a bioimaging contrast agent, but in the most of the published studies, only a limited number of dopants are described, such as Yb^{3+}/Ho^{3+}, for up-conversion luminescence under IR excitation [1-4], and Eu^{3+} as an important down-conversion red emitter in the visible light [8, 9]. Strong near infrared emitting Yb^{3+}/Er^{3+} doped fluorapatite nanoparticles was developed recently, and can be potentially more effective than Yb^{3+}/Ho^{3+} for detection of deep tissue structures, taking advantage of the near-infrared (NIR) biological window [1-3, 10]. Praseodymium ion (Pr^{3+}) doped FAP for down-conversion luminescence, which can be excited with the UV and visible light, has not been used as a dopant

for bioimaging studies. Pr^{3+} ion is chosen for the current study considering the unique optical properties, along with the tunable emission wavelengths ranging from the UV to infrared region [11]. In addition, Pr^{3+} possesses good antibacterial and antifungal characteristics and is considered as a light rare-earth element and non-toxic at the proper concentrations [12, 13]. Also, Pr^{3+} along other light rare-earth elements raised interest in recent years as an antitumor agent, because they exhibit a suppression effect on the proliferation of cancer cell lines [13, 15]. FAP nanoparticles also show anticancer properties in the studies of treatment of leukemia [16]. The promise of the combination of versatile excitation-emission profiles with excellent biocompatibility and potential anticancer properties let us to choose and design a multifunctional FAP doped Pr^{3+} contrast agent material aimed at biomedical applications.

Phosphor materials based on FAP are usually synthesized by high-temperature solid-state reaction technique for laser and luminescent tube applications [17-19]. High performances of nanomaterials for biomedical applications requires some unique structural characteristics, such as nanometer crystallite size, uniform morphology, good dispersion, and specific surface area [20]. In recent years, different classes of the stable, nontoxic and self-activated luminescent materials, with emission induced by impurities or defects in the crystal lattice have been fabricated via different synthesis routes [21]. Fluorescent fluorapatite nanoparticles for bioimaging applications, in general, are synthesized in aqueous solution, and usually have poor crystallinity, non-uniform size distributions and a tendency to easily form agglomerates [22-25]. One of the ways to overcome these problems is the thermal activation of the particles after synthesis from the aqueous solution [26-29]. In this work, we report the synthesis of novel luminescent Pr^{3+}-doped FAP nanoparticles, produced in solution followed by thermal activation, establishing a low temperature chemical production method. Usually, high temperature methods

(above 980 ^{o}C) are used for fabrication of Pr-doped FAP [18,19], but in this work we have shown that it is possible to use room temperature precipitation followed by short activation at 700 ^{o}C in order to obtain such material with prolonged time of reaction. Using this procedure, we have synthesized biocompatible and luminescent nanocrystals for bioimaging. Furthermore, we have studied the structural and optical properties of the nanocrystals, characterized the *in vitro* biocompatibility and evaluated their suitability for bioimaging applications.

2. Material and Methods

2.1 Synthesis of fluorapatite nanocrystals

The FAP and Pr^{3+} doped FAP nanocrystals were synthesized according to a co-precipitation method at room temperature (25 ^{o}C), followed by thermal activation at 700 °C. Using analytical grade chemicals, several aqueous solutions were prepared. $Ca(NO_3)_2 \cdot 4H_2O$, $Pr(NO_3)_3 \cdot 6H_2O$, $(NH_4)_2HPO_4$ and $(NH_4)F$ were dissolved in double distilled water separately. Atomic ratio of $[Pr/(Pr + Ca)] \cdot 100\%$ were 0, 0.1, 0.5 and 1% with the constant ratio (Pr + Ca)/P fixed at 1.67 in order to obtained stoichiometric FAP compounds. The solution of anions was added dropwise to a solution of cations with stirring (500 rpm), and after pH was adjusted to 10±0.5 by adding NH_4OH. After 16h of maturation, the resultant precipitates in solutions were filtered using vacuum filtration set and then washed three times with double distilled water. The slurry of precipitates was dried at 110 ^{o}C for 12h. Resultant amorphous nanomaterials were activated with calcination at 700 ^{o}C in the air for 1h. Finally, after the calcination, the obtained nanomaterials were pulverized into powder and characterized.

2.2 Characterization of fluorapatite nanoscrystals

To analyze the crystal structure of obtained powders, X-ray powder diffraction (XRPD) patterns were acquired with a Rigaku Ultima IV Japan apparatus over a 2θ range of 10°–80° using Cu Kα radiation (λ = 1.540 Å). Average crystallite size (d) was calculated by using Scherrer's formula:

$$d = 0.9\lambda/\beta \cdot \cos\theta \quad (1)$$

where λ is the wavelengths of the X-rays, θ is diffraction angle, β is corrected half-width for instrumental broadening. For the processing of X–ray powder diagram the program Powder Cell 2.4 was used.

Structure and the morphology of the samples were analyzed by transmission electron microscopy (TEM), using FEI Talos F200X microscope, operated at 200 keV. An energy dispersive X-ray spectroscopy (EDX) system attached to the TEM operating in the STEM mode was used to analyze the chemical composition of the samples.

Fourier-transform infrared spectroscopy (FTIR) spectra were recorded in the range of 4000–400 cm^{-1} using spectrophotometer (Nicolet 6700 FTIR, Thermo Scientific) and the ATR technique to obtain an infrared spectrum of absorption of the samples.

The particle size distribution was measured by dynamic light scattering (DLS) and the zeta potential of particles was determined by phase analysis light scattering and mixed mode measurement using a Zetasizer Nano ZS with MPT-2 Autotitrator Malvern Instruments, Malvern, United Kingdom.

The fluorescence properties of the nanocrystals were analyzed using a Photoluminescence spectrophotometer Horiba JovinYvon Fluoromax 4 TCSPC, and Xenon lamp

of 450 W for all excitations. The fluorescence maps of the samples were obtained in the range 350-650 nm, and spectra were measured with an integration time of 0.1 s and 1 nm slits for excitation and emission. All measurements were performed at room temperature. For each compound, a series of emission spectra were collected by excitation at different wavelengths in the range of 400–500 for doped samples, and 320–350 nm for pure FAP sample with a 3 nm step. In this way, excitation–emission matrix with dimension 11x251 is formed for each sample, which was analyzed by using the Multivariate Curve Resolution– Alternating Least Squares (MCR–ALS) method. All analyses were performed by using the unscramble software package (Camo ASA). Fluorophores of interest were extracted and fluorescence of nanocrystals was measured using excitations at wavelengths same as we used for fluorescence microscopy (405nm/488nm).

Quantum–chemical calculations were done in order to investigate the effect of replacement of Ca^{2+} ion by Pr^{3+} ion on the supramolecular structure of doped fluorapatite. The initial structure of FAP was optimized using hybrid functional B3LYP (Becke, 3-parameter, Lee–Yang–Parr) method [30], and changed structures of Pr^{3+} doped FAP were optimized using unrestricted B3LYP (UB3LYP) method. All calculations were done in Gaussian09 program (version D.01) [31], and the basis set superposition error (BSSE) was removed by counterpoise (CP) correction [32].

2.3 Cell studies

For bioimaging experiments and the study of cell viability, two different cancer cell lines were cultured. Human lung carcinoma A549 and skin carcinoma A431 cell lines were maintained in tissue culture flasks T75 at 37 °C in 5% CO_2 atmosphere. The cells were culture with DMEM

cell medium (Lonza BioWhittaker) with 4.5 g/L glucose supplemented with 10 %v/v HyClone Fetal Clone III Serum (GE Healthcare) and 1 %v/v Penicillin/Streptomycin solution.

In order to test the cell viability, cells were cultured in a 96-well plate at 5×10^3 cells/well with 100 μL complete DMEM cell medium for 24 h. Then to each well was added the control FAP and FAP-Pr^{3+} nanocrystals at concentrations of 0.5, 1, 2, 4, 8, 16, 31, 63, 125 and 250 μg/mL and incubated for 72 h. To quantify the viability, 10 μL Resazurin [33] (commercially called Alamar Blue) diluted to 0.05 mg/mL in PBS was added to each well with 100 μL cell medium, followed by 4 h incubation at 37°C. The fluorescence was read on a Microplate Reader (SynergyH1, BioTek) with excitation at 560 nm and emission 590 nm. The results were analyzed relative to the control cells without any nanoparticles added. All experiments were carried out in triplicate and three independent experiments were performed. Morphological analysis of cells lines was carried out on an optical microscope (SMZ 745, Nikon) before and after 72 hours of incubation with nanocrystals.

For the bioimaging experiments, A431 and A549 cells were plated on 8 wells μ-slides (Ibidi GmbH) with 100 μL of DMEM for 24h. After, cells were incubated for 48 h with control FAP and FAP-Pr^{3+} nanocrystals at concentrations of 125 μg/mL. After incubation the wells with cells were washed three times with Phosphate-buffered saline (PBS) to remove surplus nanocrystals, and then cells fixed with 4% Paraformaldehyde (PFA). In the end, PBS was added to each well and the cells imaged.

For widefield bioimaging studies the cells were incubated with the FAP-Pr nanocrystals. Excitation was performed with a 488 nm for the data shown in the main text and with 405 nm lasers excitation (MLC400 Monolithic Laser Combiner, Agilent) in a widefield microscope (NikonTi-E, Nikon) equipped with suited dichroics and emission filter sets (Semrock) and

detection with a sensitive EM-CCD detector (iXon 897, Andor). Widefield images were analyzed with Fiji-ImageJ.

Cell internalization of FAP-Pr nanocrystals and cytoplasm localization was characterized by fluorescence imaging using a confocal microscope (LSM780, Zeiss) and laser excitations at 488 nm. The luminescence emission was collected in the 499 to 692 nm range. Confocal z-stacks images and orthogonal view were created using Zen2010, (Zeiss) software.

3. Results and Discussion

Fluorapatite nanomaterials doped with 0.1, 0.5 and 1% of Pr^{3+} are precipitated at room temperature processing conditions, and the resulting amorphous material is calcined at 700 ^{o}C increase the luminescence intensity of Pr^{3+} ions transitions. Temperatures of 700 ^{o}C are high enough to obtain the particles with good crystallinity, good dispersion and expected emission [2, 28, 29]. Thermal treatments at 750 ^{o}C and higher, fuse the particles instead, creating the ceramic state and introducing the phase impurities.

3.1 Physico-chemical characterization

The X-ray powder diffraction (XRPD) patterns are compared with the standard FAP reference [ICSD No. 56314] and presented in Fig. 1a. All diffraction peaks can be assigned to the synthetic fluorapatite, indicating the single-phase FAP and FAP-Pr crystals with high crystallinity. Sharp characteristic peaks of the hexagonal FAP structure belong to the $P6_3/m$ space group of the apatite mineral family. This hexagonal crystal structure of apatite has good stability

and promotes stable fluorescence properties of the embedded rare-earth ions [1, 2]. Position of diffraction peaks in the region 31° to 35° shifts to higher angle values for the Pr^{3+} doped samples. Moreover, changes in lattice parameters are confirmed and expressed as a shrinkage of unit cell volume for FAP-Pr 0.1% (523.6 (2) $Å^3$) and FAP-Pr 0.5% (523.446 (3) $Å^3$) samples and little expansion for FAP-Pr 1% (525.185 (3) $Å^3$) compared to pure FAP (524.779 (3) $Å^3$) (presented in Table S1.). Values of the average crystallite size for synthesized samples calculated by Scherrer's formula were rounded to: d (FAP)=32 nm, d (FAP-Pr 0.1%)=27 nm, d (FAP-Pr 0.5%)=20 nm and d (FAP-Pr 1%)=12 nm. Decreases of crystallite size is in line with the smaller radius of Pr^{3+} ions (1,13 Å) compared to Ca^{2+} ions (1,14 Å), which are substituted in the crystal lattice [34]. Regarding the decreasing intensity of reflections and values of the average crystallite size, it can be assumed that crystallinity of the nanoparticle is slightly disturbed because Pr^{3+} substitution creates defects in the structure.

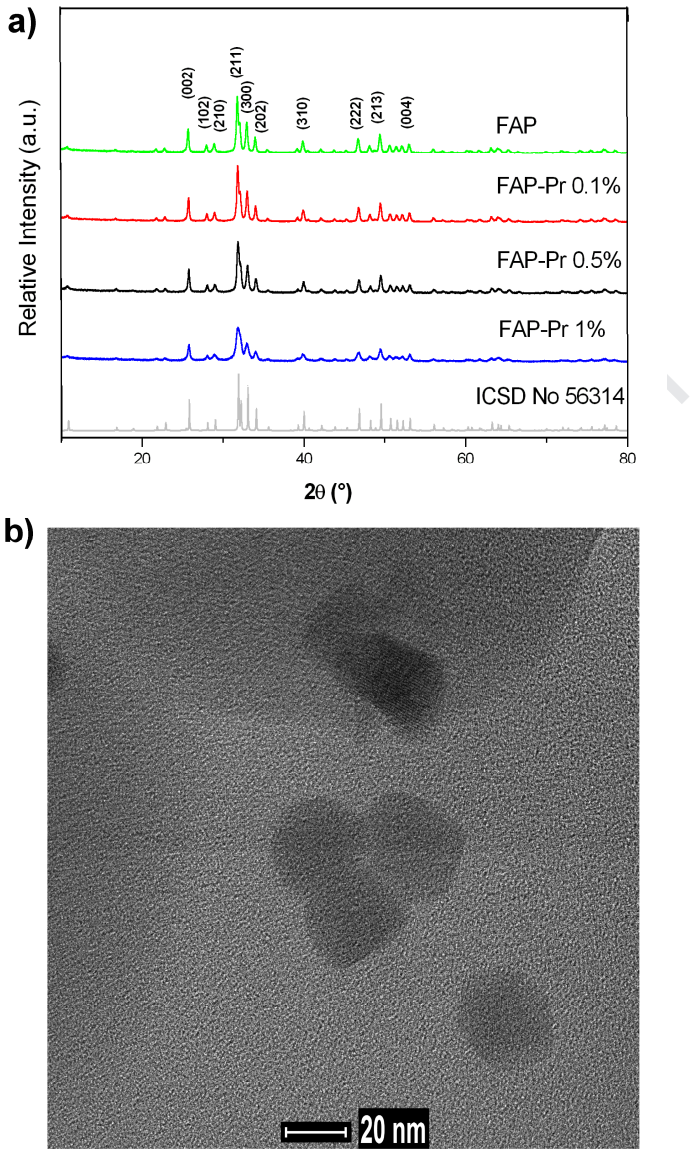

Fig. 1. Structural and morphological analysis of the FAP based nanocrystals based on X-Ray diffraction and TEM characterization. (a) The X-ray powder diffraction patterns of FAP and FAP-Pr samples. (b) TEM image of the FAP-Pr 0.5% sample.

Morphology and the particle size of FAP-Pr 0.5% nanocrystals were analyzed by transmission electron microscopy (TEM) and are presented in Fig. 1b. Spherical particles of around 20 nm could be observed, which is in good agreement with the XRD analysis. Fig. S1. shows the energy dispersive X-ray spectroscopy (EDX) mapping with spatial distribution of all elements in a sample of FAP-Pr0.5% nanocrystals. It can be seen that Pr^{3+} ions are distributed uniformly per crystals.

The Fourier-transform infrared spectroscopy (FTIR) spectra of nano-FAP powders are shown in Fig. 2, together with the characteristic vibrations of the apatite structure presented in Table S2. In the FTIR spectra the bands that appear at 1032–1095 cm^{-1} belong to the asymmetric stretch vibration of PO_4^{3-} groups (ν_3), bands at 966 cm^{-1} belong to the vibration of PO_4^{3-} groups (ν_1), while the bands at 565–603 cm^{-1} originate from stretching symmetric vibrations of PO_4^{3-} groups (ν_4). Vibrations at 752.1 and 749.0 cm^{-1} are characteristic for the incorporation of F^- ions in the apatite lattice, and are evidence that designed amounts of fluoride enter into the apatite structure [35, 36, 37].

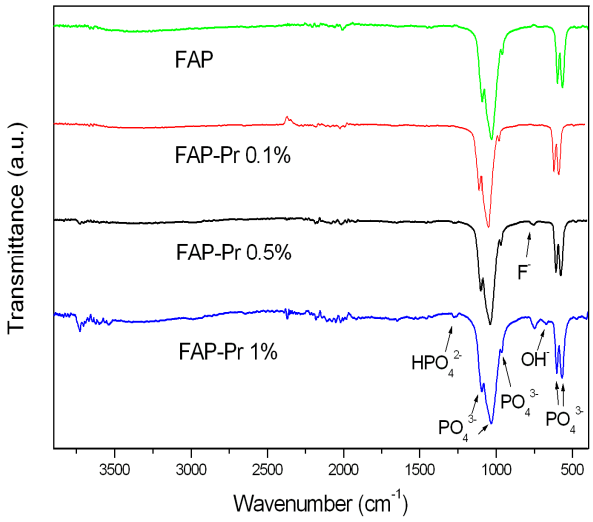

Fig. 2. FTIR spectra of FAP and FAP-Pr samples.

For the FAP-Pr 1% sample a formation of additional bands at 667.4 and 1265 cm^{-1} is characteristic for the F^- ions replacements with O-H and formation of fluoro-hydroxyapatite [36, 37]. Also, the vibration mode at 1265 cm^{-1} in some reports was assigned to the HPO_4^{2-} group which could easily substitute for phosphate ones in the apatite structure during the synthesis [37]. Considering that during the synthesis the Ca+Pr/P ratio is fixed at 1,67, to obtain stoichiometric fluorapatite compounds, the anion bands are compensated by replacing Ca^{2+} with Pr^{3+} in FAP lattice. Increasing the Pr^{3+} content and formation of the O-H bands shift the vibration of PO_4^{3-} groups to smaller values in the case of FAP-Pr 1% sample (Table S2.).

We analyze the particle size by dynamic light scattering (DLS) and zeta-potential of the FAP and FAP-Pr samples (Fig. 3a and b) in water suspension. The experimentally determined values of the surface charge is in the range of slightly negative -5 to -10 mV and of their mean sizes range between 58 and 106 nm (see Table 1). The DLS results of FAP and FAP-Pr particles confirm the nanoscale hydrodynamic size of crystals, but also the presence of aggregates. The nanocrystal sizes determines by DLS indicate the hydrodynamic radius of the nanocrystals and therefore have slightly larger values compared to the TEM determined nanocrystal diameters. In addition, some level of aggregation may be observed indicating low stability of the suspensions. The surface charge of the particles is used to determine the stability of the suspensions, and also to predict interactions with cells. FAP surface is marginally negatively charged, making the suspension more prone to be unstable. With the addition of dopants, negativity is increased, which is in accordance with the substitution of Ca^{2+} with Pr^{3+} and binding of an anion to the surface for charge compensation.

Following previous works on interactions with osteoblast cells and reparation of bone tissue [38, 39], the experimental values of surface charge and size of the fabricated FAP-Pr nanocrystal are expected to be suitable for in vitro studies and to be internalized by cells.

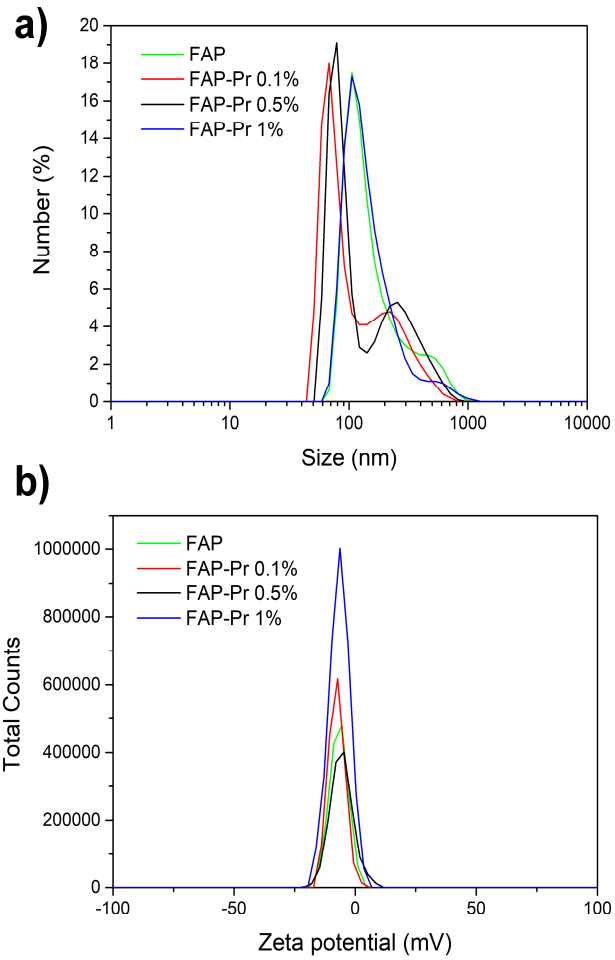

Fig. 3. Characterization of the size and surface charge of the FAP based nanocrystals. (a) DLS distribution of particle size and (b) zeta-potential of FAP and FAP-Pr samples.

Table 1

Values of mean size and zeta potential.

Sample	Mean Size (nm)	Zeta potential (mV)
FAP	105.7	-5.56
FAP-Pr 0.1%	58.77	-7.27
FAP-Pr 0.5%	78.82	-7.96
FAP-Pr 1%	105.7	-9.57

Fig. 4 shows excitation-emission profiles of synthesized samples, together with their multivariate analysis. Obtained luminescent nanocrystals of pure FAP have a fluorescence maximum in the violet region (at about 425 nm) under UV excitation (see Fig. 4a (left)). Early studies have shown that self-luminescence of FAP is the results of defects in the structure, or charge transfer (C-T) from high electronegative F^- ions [21]. Since excitation in the UV spectrum area is not suitable for biomedical and bioimaging applications, by doping Pr^{3+} ions we have tried to move both excitation and emission into the visible spectral region.

For Pr^{3+}-doped FAP crystals excitation-emission maps are collected ranging from 420 nm to 500 nm in excitation and an observation wavelength region from 520 to 680 nm (see Fig. 4b, c, d (left)). Pr^{3+}-doping results in a clear shift of the overall nanocrystal luminescence emission from the UV to the visible range, with two major bands centered at 545 nm and 600 nm.

Obtained excitation-emission map matrix is analyzed by using the Multivariate Curve Resolution-Alternating Least Squares (MCR-ALS) method [40]. This method is used to extract the number of fluorescence components which are emitted by the sample. In the case of pure FAP sample, the emission is composed of two fluorescence contributions (shown by blue and red spectra in Fig. 4a (right)). The origin of these contributions can be consequence of two types of

defects in the crystal lattice, such as hydroxyl group substitution and vacancies creation [21]. Emission of FAP samples with 0,1% and 1% Pr^{3+} also show two components (Fig. 4b and d (right)). Here, the spectrum shown in blue can be associated with the luminescence of the FAP crystal lattice, while the red spectrum originates from Pr^{3+} transitions. Only the spectrum of the FAP sample with 0.5% of Pr^{3+} dopants, shows a single dominant fluorescence contribution shown in blue, which can be associated to the Pr^{3+} transition $^1D_2 \rightarrow {}^3H_4$ (Fig. 4c (right)).

Monitoring the luminescence intensity at the emission maximum around 600 nm (transition $^1D_2 \rightarrow {}^3H_4$) we obtained the excitation spectra of Pr^{3+} in FAP host lattice, while for the undoped FAP sample the self-luminescence (charge-transfer (C-T)) is at around 425 nm (Fig. 5a). Excitation spectra for Pr-FAP samples represent the typical $4f^2 \rightarrow 4f^2$ forbidden intraconfiguration transition of Pr^{3+}. Praseodymium is very interesting as an activator ion because its energy levels contain metastable multiplet states that offer the possibility of efficient emission lines in the red, green, blue, and ultraviolet regions at different transition probabilities [41]. The energy level diagram of Pr^{3+}, which consists of a large number of energy levels is shown in Fig. 5b. We can conclude that the peaks observed in the excitation spectra of Pr^{3+} in FAP between 440 and 500 nm correspond to $^3H_4 \rightarrow {}^3P_2$, $^3H_4 \rightarrow {}^3P_1$, $^1I_6$, $^3H_4 \rightarrow {}^3P_0$ transitions (Fig. 5a). The highest intensity is detected for the FAP-Pr 0.5% sample.

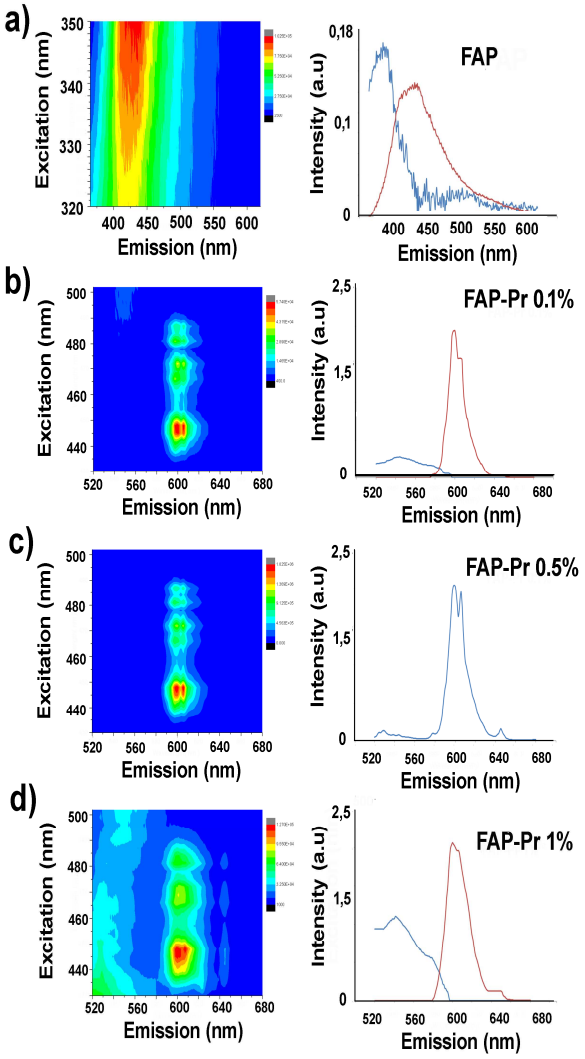

Fig. 4. Excitation-emission maps (left) and the associated two dominant fluorescence spectral contributions, blue and red spectra lines, identified by MCR-ALS (right). (a) FAP control, (b) FAP-Pr 0.1% (c) FAP-Pr 0.5% and (d) FAP-Pr 1%.

Considering that the luminescence of Pr^{3+} depends on the crystal lattice of the host, the ion concentration and the wavelength of excitation, we use resonant excitations at 488 nm and off-

resonant at 500 nm. The obtained emission spectra of FAP-Pr samples under resonant excitation are shown in Fig. 5c (emissions for off-resonant excitation can be seen at Fig. S2).

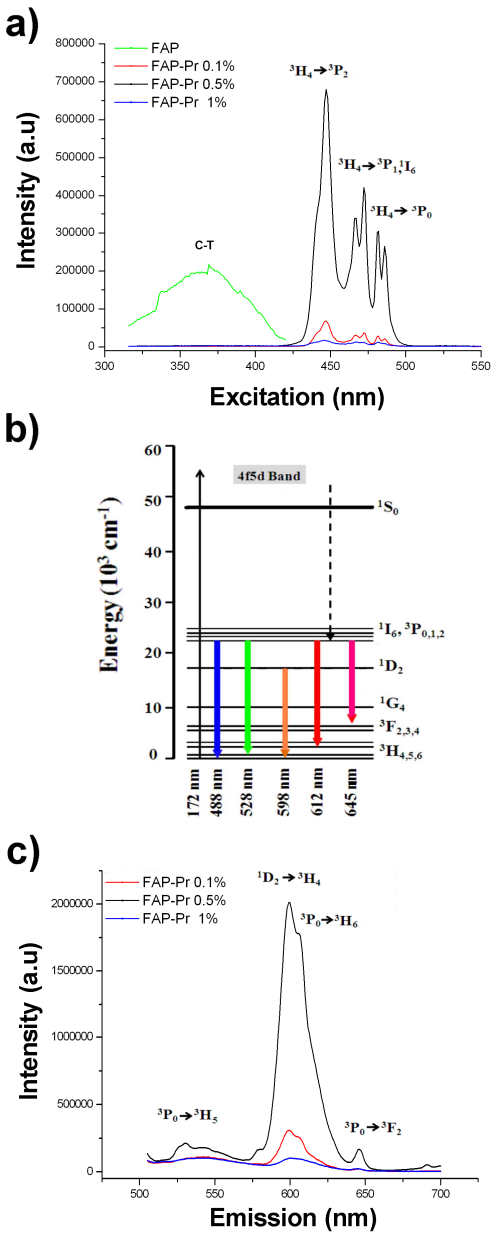

Fig. 5. Optical characterization of the FAP based nanocrystals. (a) Excitation spectra for FAP control (detected at the emission max. of 450 nm) and for FAP-Pr samples (detected at the emission max. of 600 nm). (b) The energy level diagram of Pr^{3+} ion with characteristic

transitions (modified from [41]), (c) Emission spectra of FAP-Pr samples under resonant excitations at 488 nm. The transition of Pr^{3+} ion $^1D_2 \rightarrow {}^3H_4$ (overlap $^3P_0 \rightarrow {}^3H_6$) and orange emission band at around 600 nm is predominant.

When excited with the wavelength of 488 nm, the doped FAP-Pr crystals display one dominant fluorescence emission band at about 600 nm (see Fig. 5c), associated with ($^1D_2 \rightarrow {}^3H_4$ transition of Pr^{3+} ion) accompanied with other Pr^{3+} transitions ($^3P_0 \rightarrow {}^3H_5$, $^3P_0 \rightarrow {}^3H_6$ and $^3P_0 \rightarrow {}^3F_2$) [42, 43, 44]. Resonant excitation of 488 nm excited only electrons from $^3H_4$ to $^3P_0$ accompanied with rapid non-radiative relaxations to $^1D_2$ metastable states. Considering, the transition ($^3P_0 \rightarrow {}^3H_4$) lies below on 488 nm (seen Fig. 5.b) the excitation can only relax from $^1D_2$ to $^3H_4$. As a consequence emission at 600 nm ($^1D_2 \rightarrow {}^3H_4$) is the strongest. In a previous study of the optical properties of Pr^{3+} in natural mineral fluorapatite from Spain deposits and synthetic phosphate glasses, the most intense emission band was found at about 599 and 605 nm ($^1D_2 \rightarrow {}^3H_4$ transition) for the excitation at 446 nm [42]. Moreover, in the studies of the spectroscopic properties of Pr^{3+} doped in LaF_3 nanocrystals/glass it was obtained the same two peaks that represent two possible transitions that overlap as $^1D_2 \rightarrow {}^3H_4$ + $^3P_0 \rightarrow {}^3H_6$ [44]. Transition 1D2→3H4 dominated in glass environment as a result of strong non-radiative relaxation processes of the 3P0 state. It is a possibility that the $^1D_2 \rightarrow {}^3H_4$ emission (Fig. 5c) is dominated by the strongly distorted Ca2 site formed by the change of Pr^{3+} in the crystal lattice. This dominant 600 nm orange light emission is the most intense for FAP-Pr 0.5% sample and the smallest for FAP-Pr 1%. Earlier research has shown that emission from the $^1D_2$ states to the $^3H_4$ state is very sensitive to the dopant ion concentration, their arrangement in structure, as well as the phonon

energy of the crystal lattice [43, 45]. Emission intensity drops sharply as Pr^{3+} concentration increases, and this phenomenon has been attributed to cross-relaxation between neighboring Pr^{3+} ions [43, 45]. This is in correlation with the smaller emission intensity for FAP-Pr 1% sample with the highest dopant concentration. The distance between Pr^{3+} ions decreases as the concentration increases, so cross-relaxation becomes more frequent. In order to increase the luminescence intensity of materials, the addition of the second dopant to create charge transfer is needed [1-4, 26]. Earlier studies have shown that the appearances of OH^- ions in the FAP crystal lattice leads to a decrease in the intensity of luminescence, which is one of the reasons why the FAP sample with 0.5% Pr has the highest luminescence [45, 46].

Overall, the results show the emission of nanocrystals depends on dopant concentration and luminescence efficiency is maximal for FAP-Pr 0.5%, which is selected for luminescence-based in vitro cell studies.

3.2 Quantum-chemical calculations of the structural changes in FAP crystal

In FAP crystals Ca^{2+} ions are placed in two different crystallographic symmetry position, Ca1 (*4f*) and Ca2 (*6h*), both are available for substitution with rare earth Pr^{3+} ions [46]. The nine–fold coordinated Ca1 site, with a C_3 local symmetry, is connected to six phosphate groups. The seven–fold coordinated Ca2 site with a C_s local symmetry, is connected to five phosphate groups and one fluoride anion [46]. The site–occupancy ratios of individual rare earth elements (REE) to Ca1 and Ca2 sites (REE–Ca2/REE–Ca1) for the natural REE–bearing fluorapatite samples were previously calculated by using the measured and interpolated ratios for the single–REE substituted fluorapatite sample [47]. The evaluated value of site occupancy ratio for

praseodymium is 3.22, and indicates a dominant preference for Ca2 site. The earlier study of site preference of rare earth elements in fluorapatite from the same authors [48], have also shown that Pr^{3+} substituted Ca^{2+} in Ca2 site.

In the present work, quantum–chemical calculations are performed to investigate the effect of replacement of Ca^{2+} by Pr^{3+} ion in site Ca2 on the supramolecular structure of doped fluorapatite. Initial structure for calculations, corresponding to close environment of fluoride ions, is taken from the crystal structures of fluorapatite [49]. The structure contains fluoride ion, three Ca^{2+} ions (located at Ca2 site) and three phosphate ions. For simplicity, this system is marked as FAP fragment. The initial structure is optimized using B3LYP method, SDD basis set form Ca^{2+} ions and 6–31g basis set for other elements. The geometry of optimized FAP fragment (Fig. 6a) shows a good agreement with the geometry of the fragment found in the crystal structure (fluoride ions are also located in plane formed by Ca^{2+} ions, at distances of 2.31 Å from each of them; Ca^{2+} ions are separated by a distance of 4.00 Å). This agreement indicates a reliable level of theory. The optimized FAP fragment is used as the starting structure, in which Ca^{2+} ions are replaced by Pr^{3+} ions. The changed structures are further optimized using unrestricted B3LYP (UB3LYP) method, SDD basis set for metal ions and 6–31g basis set for other atoms. Unrestricted B3LYP method was chosen because the Pr^{3+} contains unpaired electrons.

Replacement of Ca^{2+} with Pr^{3+} ions leads to a distortion of the structure of the doped fluorapatite nPr–FAP systems, where n is the number of Ca ions replaced by Pr ions and compared to the structure of the optimized FAP fragment (Fig. 6a). The distortion is described by parameters describing the distances between the respective atoms and planes as shown in Fig. 6b, while the determined values of these parameters are given in Table S3.

The introduction of Pr^{3+} ions in the FAP–system leads to increasing repulsive forces between metal ions, and to increased M···M distances (from 3.89 Å in FAP to 4.02 Å in 3Pr–FAP system). These changes are accompanied by increasing of M···O distances (from 2.25 Å in FAP to 2.48 Å in 3Pr–FAP system) and deviation of F^- ion from the plane formed by metal ions (R parameter). Based on the results of calculations, it should be expected the increase in unit cell parameters of doped samples (especially the volume, V), which can be confirmed by the data obtained from XRD. Namely, there is the increase of unit cell parameters for doped sample (for example for 1% doped sample a=9.38533 (3) Å, c=6.88465 (3) Å, and V=525.185 (3) $Å^3$) as compared to parameters for FAP (a=9.3775 (3) Å, c=6.8910 (2) Å, and V=524.779 (3) $Å^3$). A growing number of Pr^{3+} ions in the nPr–FAP system leads to a slight reduction of the R deviation (0.97 Å in Pr–FAP, 0.95 Å in 2Pr–FAP, and 0.88 Å in 3Pr–FAP system) and to increased attractive forces between the positively charged metal ions and negatively charged phosphate and fluoride ions. A reduction of the system volume is the result of these changes (485.88 $Å^3$ for Pr–FAP, 479.29 $Å^3$ for 2Pr–FAP, and 472.79 $Å^3$ for 3Pr–FAP system), which is consistent with the results for volume reduction obtained from X-ray powder diffraction analysis for the samples FAP, FAP-Pr0.1% and FAP-Pr0.5%. For the sample FAP-Pr1% it should be expected the decrease of luminescence intensity.

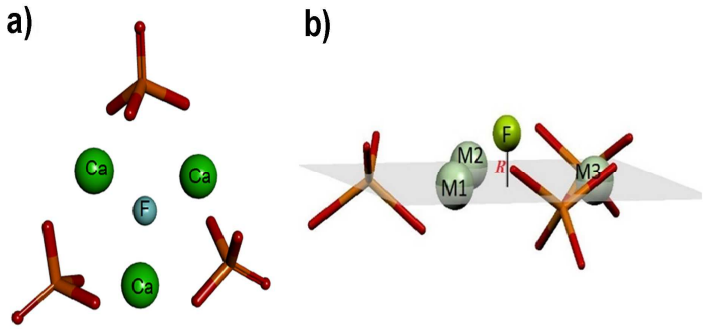

Fig. 6. Theoretical structural analysis. (a) The optimized structure of the FAP fragment, extracted from crystal structure using B3LYP method. The fluoride ion is located in the plane formed by Ca^{2+} ions, equidistant from each of them (a distance of 2.25 Å). Ca^{2+} ions are separated by a distance of 3.89 Å. The phosphate ions simultaneously interact with two Ca^{2+} ions, with the first interacts via two oxygen atoms (bifurcated interaction), while with the second one via a single oxygen atom (monofurcated interaction). (b) Illustration of parameters that are used to describe the structure of the nPr–FAP system (optimized by UB3LYP method), where M1 to 3 represent the Ca ion sites to be replaced partially by Pr ions.

On the basis of the analysis, prediction of structural changes by quantum–chemical calculations, replacement of Ca^{2+} ion with Pr^{3+} ion leads to distortion in the structure of the doped fluorapatite. These changes are accompanied by increasing of M···O distances and deviation of F^- ion from the plane formed by metal ions. The FTIR spectrum (Fig. 2) shows that with the increase in Pr^{3+} concentration O-H vibrations occur, but only fluorapatite phases are observed in the XRD patterns (Fig. 1a). Increasing the Pr^{3+} ion concentration increases the amount of OH^- ions, which is accompanied by the transfer of the proton from OH^- groups to the PO_4^{2-} group (HPO_4^{2-} ions are generated (Fig. 2)). In this way, the negative charge is increased

(the OH group is charged -1, and O ion -2) and thereby the electrostatic force between Pr and O atoms, which additionally stabilizes the structure.

Overall, based on the performed structural analysis the assumed substitution mechanism is one Pr^{3+} for one Ca^{2+}, with partial substitution of F^{-} with O^{2-} and OH^{-} and creation of ionic vacancy due to charge balances. Increasing of Pr^{3+} concentrations in FAP, with appearances of OH^{-} and vacancy's, leads to the luminescence quenching.

3.3 Biocompatibility of FAP-Pr nanoparticles

It is important for any nanoparticle candidate for bioimaging applications to show no toxicity and high biocompatibility. We compared the cytotoxicity of the three types of FAP-Pr nanomaterials with 0.1%, 0.5%, 1% of Pr^{3+} in addition to the FAP control sample. The proliferation of two cancer cell lines A549 and A431 incubated with different concentrations of FAP and FAP-Pr nanocrystals for 72 h is evaluated using the Resazurin cell viability assay [33]. Fig. 7a and b show that cell proliferation for both cell lines with the different dosage groups display a normal growth trend, even at a high dosage of 240 μg/mL. All experimental groups show viability comparable to the control with cells only. This result indicates no evident cytotoxicity of the FAP-Pr doped nanocrystals in the tested conditions, allowing for live-cell imaging studies.

Additionally, morphological observation of cells was carried out on the optical microscope before and after 72 h of incubation with nanocrystals. Fig. 7c shows the morphology of A549 without nanocrystals and after they are incubated with 125 μg/mL of FAP-Pr 0.5% for

72 h. Also, the same for A431, with cells only and cells with 250 µg/mL of FAP-Pr 1% (Fig. 7d). In both cases, it can be seen that all cells retained normal morphology.

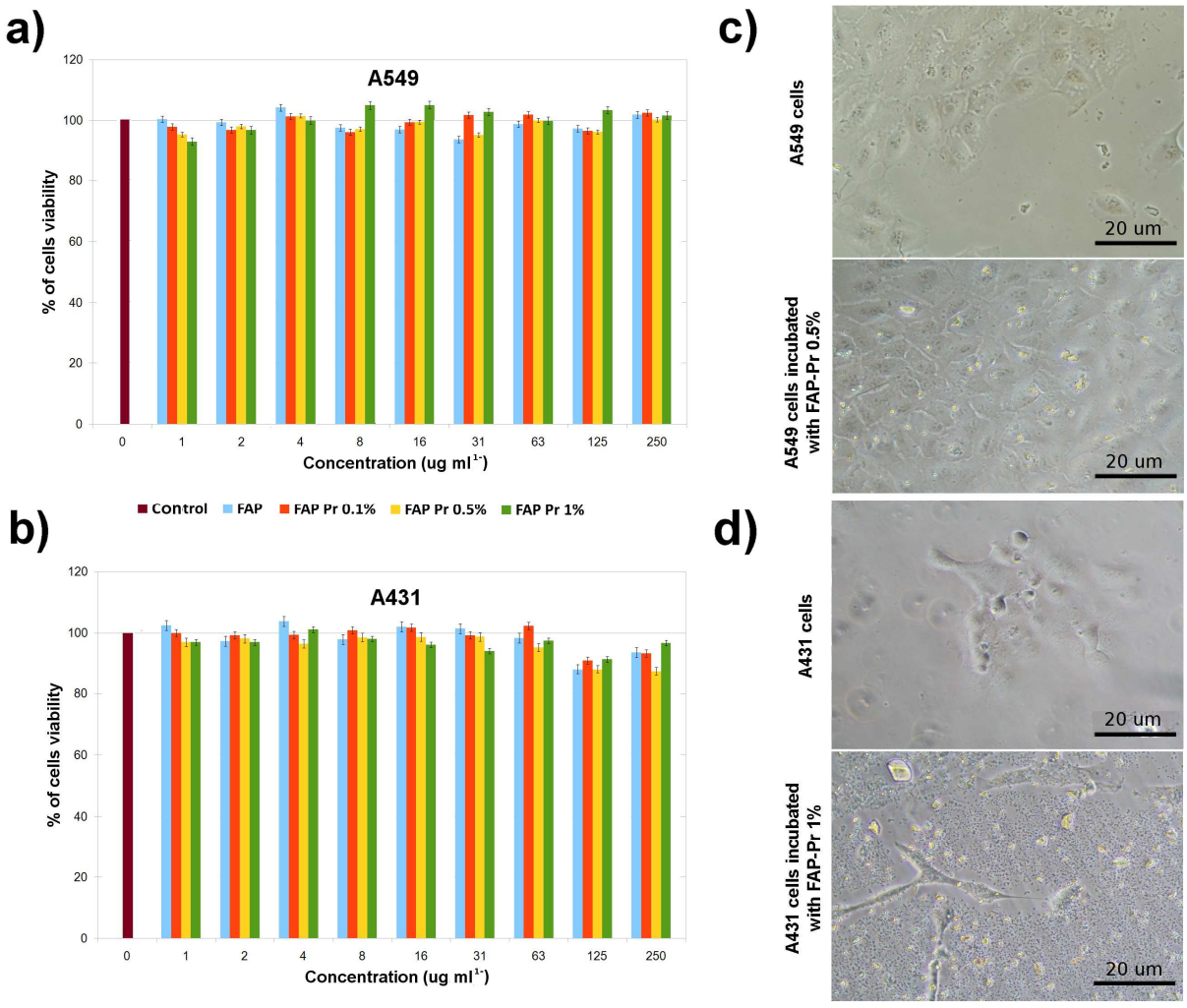

Fig. 7. In vitro cytotoxicity study of the FAP and FAP-Pr samples with 0.1, 0.5 and 1% Pr^{3+}. The cells were incubated with the nanoparticles for 72h at 37 ^{0}C, resazurin viability assay was performed and results normalized to control cells with no treatment. (a) Cell viability of A549 cells and (b) A431 cells incubated with different concentration of FAP and FAP-Pr nanocrystals.

Transmission images showing morphologies of (c) A549 cells without nanocrystals (top) and cells incubated with 125 μg/mL FAP-Pr 0.5% (bottom); (d) A431 cells without nanocrystals (top) and cells incubated with 250 μg/mL of FAP-Pr 1% (bottom).

The viability assay and cell morphological results indicate that the FAP-Pr nanocrystals with different doped amounts of Pr^{3+} ions are biocompatible and nontoxic to live cells, hence promising candidates for biological applications. These results are in agreement with studies of cytotoxicity of FAP doped with different rare-earth ions, with reported cell viabilities up to 90% [26]. As we already mentioned, Pr^{3+} is a light rare-earth element and earlier research demonstrated good biocompatibility, this was connected to the poor solubility of praseodymium [13].

3.4 Cell uptake of FAP-Pr nanoparticles

Based on the excellent biocompatibility and optical properties of the FAP-Pr nanocrystals, cell imaging studies were performed to evaluate the potential for biomedical applications. The nanocrystals were incubated for 48 h with the A431 cells. To confirm cell uptake and luminescence of the nanocrystals inside cells, widefield and confocal fluorescence microscopy is used. In Fig. 8a widefield images are shown for A431 cells incubated with FAP-Pr 0.5% nanocrystals, compared to control cells with no added nanoparticles. The observable fluorescence intensity spots upon 488 nm excitation suggest the FAP-Pr 0.5% nanocrystals are located inside the cells. The obtained luminescence at 488 nm was stable for several hours. Fluorescent images under 405 nm excitation are presented in Fig. S2.

To confirm if the fluorescent FAP-Pr 0.5% material is indeed internalized by the cells, confocal z-stacks of cells were acquired and analyzed. In Fig. 8b individual slices across the cell with 2 μm separation in the axial direction are shown together with the orthogonal projection (Fig. 8c).

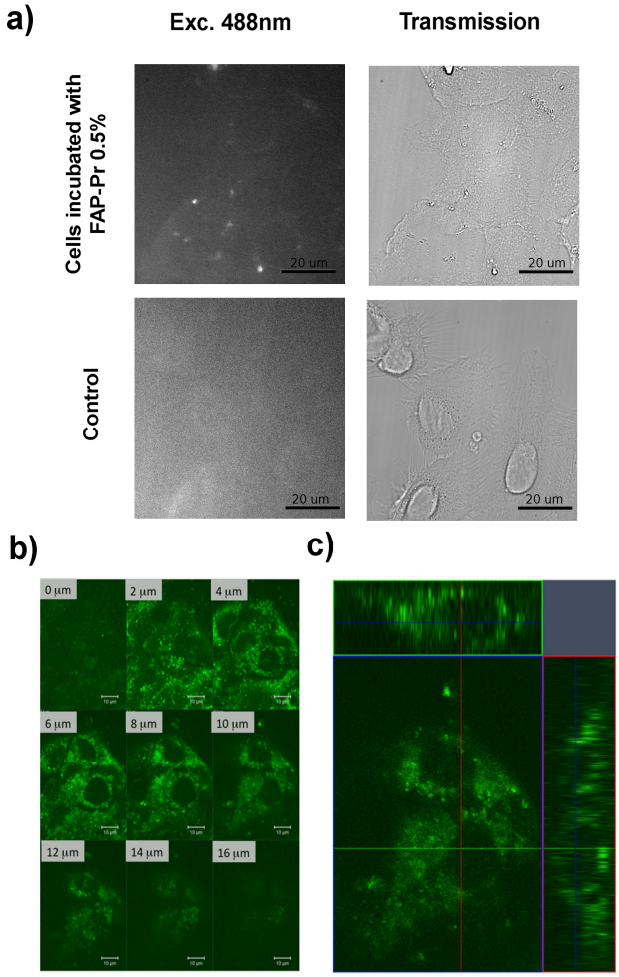

Fig. 8. Analysis of the cell internalization of FAP-Pr 0.5% nanocrystals. (a) Fluorescence widefield images of A431 cells taken under 488 nm laser excitation (left) and corresponding transmission image (right) after 72h incubation with FAP-Pr 0.5% (top) and control cells without

nanocrystals (bottom). Confocal fluorescence images of A431 cells incubated with FAP-Pr 0.5%, (b) optical slices at selected z-heights and (c) orthogonal projection at the 6 μm height.

The optical sectioning of the confocal microscope allows to address ellipsoidal voxels of about < 500 nm x 500 nm x 1 μm, a volume that is much smaller compared to the cellular extension and allows to address the cell interior without signal contributions from the cell wall or cell exterior. The 2 μm slice is taken at the coverslip surface and one can see that the nanocrystals are found dispersed on the surface (Fig. 8b). Moving the focus up to the 4/6/8/10/12 and 14 μm slices above the coverslip, the observed signal is from nanocrystals that entered the cell and are positioned inside the cytoplasm. This is verified by the respective orthogonal cross section views, shown in Fig. 8c, where it can be seen that the nanocrystal signal is distributed along the z axial direction in the cell cytoplasm.

The imaging data follows previous findings of cellular uptake for the internalization of different nanoparticles showing predominant delivery of the particles into the cell cytoplasm [50]. Dominant mechanisms for nanoparticles uptake include clathrin-dependent mechanisms (receptor-mediated endocytosis), macropinocytosis, and phagocytosis [51].

Overall, our results indicate that the nanocrystal FAP-Pr 0.5% are able to be internalized by cells and detected by imaging, though the luminescent signal intensity is low. Nevertheless, the material is promising for nanoparticle based labeling and tracking of cells in both *in vitro* and *ex vivo* tissue slices bioimaging applications. The FAP-Pr 0.5% excitation and emission wavelengths are widely available is most microscopy systems. Additionally the 600 nm emission

is an advantage, because is out of the green autofluorescence window of the tissue, enabling for lower levels of background.

Future studies should focus on increasing the intensity of luminescence of nanocrystals, which can be achieved by increasing dopant concentration with addition of the second dopant taking into account the need of a monovalent charge, to keep the charge balance in the crystal material [52]. Furthermore, the use of alternative dopants with emission peaks at longer wavelengths shall be considered to ideally reach into the biological window in the near infrared spectral region (800-950nm).

Additionally, multimodal imaging in combining fluorescent and magnetic imaging modalities can provide synergistic advantages for non-invasive medical diagnosis. Considering Pr has paramagnetic properties [53], FAP-Pr nanocrystals can be a potential contrast agent for MRI imaging. Compared to typical Gd-based agents, biocompatibility of FAP matrix doped with Pr is a high advantage [52].

4. Conclusion

New single phase FAP-Pr nanocrystals were synthesized using a room temperature co-precipitation method followed by calcination. The XRD, FTIR and theoretical analysis show that in hexagonal FAP crystal lattice Pr^{3+} is positioned at Ca2 (*6h*) sites, with partial substitution of F^- with O^{2-} and OH^- and creation of vacancy due to charge balances. The nanoscale properties of the crystals were evaluated by TEM and DLS analysis, and EDX mapping elemental composition analysis. The luminescence properties of FAP-Pr nanocrystals show that at 0.5% of Pr^{3+} concentration in the FAP lattice the luminescence intensity is highest with well separated

green and orange luminescence transitions. At increasing Pr^{3+} concentrations crystallite size decreases while the cross-relaxation between neighbor ions increases, which leads to luminescence quenching.

The new FAP-Pr nanocrystals have excellent biocompatibility and are successfully taken up by cells as demonstrated using two different cancer cell models. Widefield and confocal fluorescence imaging results show luminescence signal from inside the cells, confirming that the nanocrystals entered the cell and are positioned in the cytoplasm. As a contrast agent in bioimaging applications, the intensity of the nanocrystals needs to be increased to achieve facile detection suited to enter into translational biomedical research and/or clinical applications. Though the material is promising, several potential uses could emerge from this material, including detection, tracking, delivery and therapy applications associated with cancer as well musculoskeletal diseases.

Conflicts of interest

"There are no conflicts to declare".

Acknowledgement

Financial support by the European Cooperation in Science and Technology through COST Action MP1302 Nanospectroscopy for Dušan V. Milojkov STSM visit to INL is gratefully acknowledged. The INL team acknowledges financial support by the CCDR-N via the grant: NORTE-01-0145-FEDER-000019. Oscar F. Silvestre received a Marie Curie fellowship, EU-EC COFUND programme "NanoTRAINforGrowth" (grant no. 600375). Acknowledge of co-authors from Serbia to their projects No. III 43009, III 45021, OI 172023, OI 173017, supported by the

Ministry of Education, Science and Technological Development of the Republic of Serbia. Numerical simulations were run on the PARADOX supercomputing facility at the Scientific Computing Laboratory of the Institute of Physics Belgrade, supported in part by the Ministry of Education, Science and Technological Development of the Republic of Serbia.

References

[1] S. S. Syamchand, G. Sony, Fluorescein-labeled fluoroapatite nanocrystals codoped with Yb(III) and Ho(III) for trimodal (downconversion, upconversion and magnetic resonance) imaging of cancer cells, Microchim. Acta. 183(12) (2016) 3209–3219. https://doi.org/10.1007/s00604-016-1970-9

[2] X. Li, J. Zhu, Z. Man, Y. Ao, H. Chen, Investigation on the structure and upconversion fluorescence of Yb^{3+}/Ho^{3+} co-doped fluorapatite crystals for potential biomedical applications Sci. Rep. 4(1) (2015) 4446. https://doi.org/10.1038/srep04446

[3] X. Hu, J. Zhu, X. Li, X. Zhang, Q. Meng, L. Yuan, J. Zhang, X. Fu, X. Duan, H. Chen, Y. Ao, Dextran-coated fluorapatite crystals doped with Yb^{3+}/Ho^{3+} for labeling and tracking chondrogenic differentiation of bone marrow mesenchymal stem cells in vitro and in vivo, Biomaterials. 52 (2015) 441–451. https://doi.org/10.1016/j.biomaterials.2015.02.050

[4] Y. Xie, Y. Xie, W. He, F. Li, T. S. H. Perera, L. Gan, Y. Han, X. Wang, S. Li, H. Dai, Luminescence Enhanced Eu^{3+}/Gd^{3+} Co-Doped Hydroxyapatite Nanocrystals as Imaging Agents In Vitro and In Vivo, ACS App. Mater. Inter. 8(16) (2016) 10212–10219. DOI: 10.1021/acsami.6b01814

[5] J. Liu, T. Jin, S. Chang, A. Czajka-Jakubowska, Z. Zhang, J. E. Nö, B. H. Clarkson, The Effect of Novel Fluorapatite Surfaces on Osteoblast-Like Cell Adhesion, Growth, and Mineralization,Tissue. Eng.: Part A. 16(9) (2010) 2977. DOI: 10.1089/ten.tea.2009.0632

[6] K. Tanimoto, T. Le, L. Zhu, J. Chen, J.D.B. Featherstone, W. Li, P. D. Besten, Effects of Fluoride on the Interactions between Amelogenin and Apatite Crystals, J. Dent. Res. 87(1) (2008) 39–44. doi: 10.1177/154405910808700106

[7] B. Basu, S. Ghosh, Biomaterials for Musculoskeletal Regeneration; Springer: Bangalore, India, 2017; ISBN 9789811030581.

[8] Jun Xu, X. Shen, L. Jia, Z. Xu, T. Zhou, X. Li, T. Ma, H. Li, Y. Wang, T. Zhu, Facile synthesis of folic acid-conjugated fluorapatite nanocrystals for targeted cancer cell fluorescence imaging, Mater. Lett. 203 (2017) 37–41.

[9] H. F. Zeng, M. Y. Sun, S. F. Wu, H. F. Chen, Synthesis of Europium-doped Fluorapatite Nanorods and Their Multifunctional Biomedical Applications, Molecules. 22 (2017) 753. doi:10.3390/molecules22050753

[10] S. Karthi, G. S. Kumar, G. A. Kumar, D. K. Sardar, S. Chidangil, E. K. Girija, Microwave assisted synthesis and characterizations of near infrared emitting Yb/Er doped fluorapatite nanoparticles, J. Alloys Compd. 689 (2016) 525-532, doi: 10.1016/j.jallcom.2016.08.005.

[11] D. K. Sardar, F. S. Salinas, R. M. Yow, Stark effects on the spectra of trivalent praseodymium ions in strontium fluorapatite laser host, J. Appl. Phys. 88(8) (2000) 4688.

[12] S. Singh, O. Pandey, S. Sengupta, Microwave assisted synthesis, spectroscopy and biochemical aspects of lanthanum (III) and praseodymium (III) complexes with oxadiazole functionalised dithiocarbazinates, J. Rare Earth. 27(5) (2009) 698–704. DOI: 10.1016/S1002-0721(08)60319-1

[13] F. Feyerabend, J. Fischer, J. Holtz, F. Witte, R. Willumeit, H. Drücker, C. Vogt, N. Hort, Evaluation of short-term effects of rare earth and other elements used in magnesium alloys on primary cells and cell lines, Acta. Biomater. 6(5) (2010) 1834–1842. DOI: 10.1016/j.actbio.2009.09.024

[14] Y. Liu, S. Tian, S. Liu, E. Wang, In vitro inhibitory effect of polyoxometalates on human tumor cells, Transit. Metal. Chem. 30(1) (2005) 113–117. DOI: 10.1007/s11243-004-3825-1

[15] Y. J. Ji, B. Xiao, Z. H. Wang, M. Z. Cui, Y. Y. Lu, The suppression effect of light rare earth elements on proliferation of two cancer cell lines, Biomed Environ Sci. 13 (2000) 287–92.

[16] M. Theiszova, S. Jantova, S. Letasiova, M. Palou, L. Cipak, Cytotoxicity of hydroxyapatite,fluorapatite and fluor– hydroxyapatite: a comparative in vitro study, Neoplasma. 55(4) (2008) 312–316.

[17] M. Gaft, R. Reisfeld, G. Panczer, E. Uspensky, B. Varrel, G. Boulon, Luminescence of Pr^{3+} in minerals, Opt. Mater. 13 (1999) 71–79.

[18] J. Yang, L. Shen, E.Y. Bun Pun, H. Lin, Superiority of shortwave transparent glasses with moderate phonon energy in achieving effective radiations from $^1D_2$ level of Pr^{3+}, J. Lumin. 213 (2019) 51–60, doi: https://doi.org/10.1016/j.jlumin.2019.05.008.

[19] D. K. Sardara, C. C. Russell, Optical transitions, absorption intensities, and intermanifold emission cross sections of Pr^{3+}(4f2) in $Ca_5(PO_4)_3F$ crystal host, J. Appl. Phys., 95(10) (2004) 5334–5339. https://doi.org/10.1063/1.1690092

[20] C. S. Ciobanu, S. L. Iconaru, F. Massuyeau, L. V. Constantin, A. Costescu, D. Predoi, Synthesis, Structure, and Luminescent Properties of Europium-Doped Hydroxyapatite

Nanocrystalline Powders, Journal of Nanomaterials, J. Nanomater. Vol. 2012, Article ID 942801, 9. http://dx.doi.org/10.1155/2012/942801

[21] C. Zhang, J. Lin, Defect-related luminescent materials: synthesis, emission properties and applications, Chem. Soc. Rev. 41 (2012) 7938–7961. DOI 10.1039/C2CS35215J

[22] Y. Sun, H. Yang, D. Tao, Preparation and characterization of Eu3+-doped fluorapatite nanoparticles by a hydrothermal method, Ceram. Int. 38 (2012) 6937–6941. DOI: 10.1016/j.ceramint.2012.05.036

[23] L. Zhang, Z. Fu, Z. Wu, Y. Wang, X. Fu, T. Cui, Investigation of structural and luminescent properties of Ce^{3+}/Mn^{2+} ions-doped $Ca_5(PO_4)_3F$, Mater. Res. Bull. 56 (2014) 65–70. DOI: 10.1016/j.materresbull.2014.04.032

[24] X. Yan, Z. Fu, X. Wang, J. H. Jeong, Hidrothermal synthesis and luminescence properties of $Ca_5(PO_4)_3F:Eu^{3+}$ microrods, J. Lumin. 152 (2014) 226–229.

https://doi.org/10.1016/j.jlumin.2013.10.029

[25] A. Doat, F. Pellé, N. Gardant, A. Lebugle, Synthesis of luminescent bioapatite nanoparticles for utilization as a biological probe, J. Solid State Chem. 177 (2004) 1179–1187. doi:10.1016/j.jssc.2003.10.023

[26] S. Karthi, G. A. Kumar, D. K. Sardar, C. Santhosh, E. K. Girija, Synthesis and characterization of $Nd^{3+}:Yb^{3+}$ co-doped near infrared sensitive fluorapatite nanoparticles as a bioimaging probe, Opt. Mater. 77 (2018) 39–47. https://doi.org/10.1016/j.optmat.2018.01.013

[27] X. Zheng, M. Liu, J. Hui, D. Fan, H. Ma, X. Zhang, Y. Wang, Y. Wei, Ln^{3+}-doped hydroxyapatite nanocrystals: controllable synthesis and cell imaging, Phys. Chem. Chem. Phys. 17 (2015) 20301. DOI: 10.1039/c5cp01845e

[28] P. Sobierajska, K. Zawisza, R. M. Kowalski, G. Renaudin, J.-M. Nedelec, J. Zienkiewicz, R. J. Wiglusz, Preparation of up-converting nano-biphasic calcium phosphate, RSC Adv. 7 (2017) 30086–30095. DOI: 10.1039/C7RA04809B

[29] J. Hui, X. Zhang, Z. Zhang, S. Wang, L. Tao, Y. Wei, X. Wang, Fluoridated HAp:Ln^{3+} (Ln 1⁄4 Eu or Tb) nanoparticles for cell-imaging, Nanoscale. 4 (2012) 6967. DOI: 10.1039/c2nr32404k

[30] A. D. Becke, A new mixing of Hartree–Fock and local density□functional theories, J. Chem. Phys. 98 (1993) 1372. https://doi.org/10.1063/1.464304

[31] M. J. Frisch, G. W. Trucks, H. B. Schlegel, G. E. Scuseria, M. A. Robb, J. R. Cheeseman, G. Scalmani, V. Barone, B. Mennucci, G. A. Petersson, H. Nakatsuji, M. Caricato, X. Li, H. P. Hratchian, A. F. Izmaylov, J. Bloino, G. Zheng, J. L. Sonnenberg, M. Hada, M. Ehara, K. Toyota, R. Fukuda, J. Hasegawa, M. Ishida, T. Nakajima, Y. Honda, O. Kitao, H. Nakai, T. Vreven, J. A. Montgomery, Jr. Peralta, J. E. F. Ogliaro, M. Bearpark, J. J. Heyd, E. Brothers, K. N. Kudin, V. N. Staroverov, R. Kobayashi, J. Normand, K. Raghavachari, A. Rendell, J. C. Burant, S. S. Iyengar, J. Tomasi, M. Cossi, N. Rega, N. J. Millam, M. Klene, J. E. Knox, J. B. Cross, V. Bakken, C. Adamo, J. Jaramillo, R. Gomperts, R. E. Stratmann, O. Yazyev, A. J. Austin, R. Cammi, C. Pomelli, J. W. Ochterski, R. L. Martin, K. Morokuma, V. G. Zakrzewski, G. A. Voth, P. Salvador, J. J. Dannenberg, S. Dapprich, A. D. Daniels, Ö . Farkas, J. B. Foresman, J. V. Ortiz, J. Cioslowski, D. J. Fox, Gaussian, Inc., Wallingford CT, 2009.

[32] S. F. Boys, F. Bernardi, The calculation of small molecular interactions by the differences of separate total energies. Some procedures with reduced errors, Mol. Phys. 9 (4) (1970) 1553−1566. https://doi.org/10.1080/00268977000101561

[33] S. N. Rampersad, Multiple Applications of Alamar Blue as an Indicator of Metabolic Function and Cellular Health in Cell Viability Bioassays, Sensors. 12(12) (2012) 12347–12360. DOI: 10.3390/s120912347

[34] R. D. Shannon, Revised Effective Ionic Radii and Systematic Studies of Interatomic Distances in Halides and Chalcogenides, Acta Cryst. A32 (1976) 751-767.

[35] A. Serret, M. V. Cabañas and M. Vallet-Regí, Stabilization of Calcium Oxyapatites with Lanthanum(III)-Created Anionic Vacancies, Chem. Mater. 12 (2000) 3836–3841. DOI: 10.1021/cm001117p

[36] Y. Huang, G. Song, X. Chang, Z. Wang, X. Zhang, S. Han, Z. Su, H. Yang, D. Yang, X. Zhang, Nanostructured Ag^{+}-substituted fluorhydroxyapatite-TiO_2 coatings for enhanced bactericidal effects and osteoinductivity of Ti for biomedical applications, Int. J. Nanomed. 13 (2018) 2665–2684. doi: 10.2147/IJN.S162558

[37] E. M. Zahrani, M. H. Fathi, The effect of high-energy ball milling parameters on the preparation and characterization of fluorapatite nanocrystalline powder, Ceram. Int. 35 (2009) 2311–2323. doi:10.1016/j.ceramint.2009.01.012

[38] T. Guo, Y. Li, G. Cao, Z. Zhang, S. Chang, A. Czajka–Jakubowska, J.E. Nör, B.H. Clarkson and J. Liu, Fluorapatite-modified scaffold on Dental pulp stem cell Mineralization, J. Dent. Res. 93 (2014) 1290–1295. DOI: 10.1177/0022034514547914

[39] K. Cheng, W. Weng, H. Wang, S. Zhang, In vitro behavior of osteoblast-like cells on fluoridated hydroxyapatite coatings, Biomaterials. 26 (2005) 6288–6295. https://doi.org/10.1016/j.biomaterials.2005.03.041

[40] J. Mendieta, Multivariate curve resolution: a possible tool in the detection of intermediate structures in protein folding, Biophys. J. 74 (1998) 2876–2888. doi:10.1016/S0006-3495(98)77994-9

[41] Y. Chen, J. Wang, C. Liu, J. Tang, X. Kuang, M. Wu, Q. Su, UV-Vis-NIR luminescence properties and energy transfer mechanism of $LiSrPO_4:Eu^{2+}$, Pr^{3+} suitable for solar spectral convertor, Opt. Express. 21 (2013) 3161–9. https://doi.org/10.1364/OE.21.003161

[42] S. Bodyl, Optical properties of Pr^{3+}, Sm^{3+} and Er^{3+} ions in apatite, fluorite and phosphate glasses, Physics Procedia. 2 (2009) 515-525. http://dx.doi.org/10.1016/j.phpro.2009.07.037

[43] Y.-C. Li, Y.-H. Chang, Y.-F. Lin, Y.-S. Chang, Y.-J. Lin, Luminescent properties of trivalent praseodymium-doped lanthanum aluminum germanate $LaAlGe_2O_7$, J. Phys. Chem. Solids. 68 (2007)1940-1945. http://dx.doi.org/10.1016/j.jpcs.2007.06.013

[44] X.-j. Wang, S. H. Huang, R. Reeves, W. Wells, M.J. Dejneka, R.S. Meltzer, W.M. Yen, Studies of the spectroscopic properties of Pr^{3+} doped LaF_3 nanocrystals/glass, J. Lumin. 94–95 (2001) 229–233.

[45] V. Naresh, B. S. Ham, Influence of multiphonon and cross relaxations on $^3P_0$ and $^1D_2$ emission levels of Pr^{3+} doped borosilicate glasses for broad band signal amplification, J. Alloys Compd. 664 (2016) 321-330, doi: 10.1016/j.jallcom.2015.12.246.

[46] P. Sobieraj, R. Pazik, K. Zawisza, G. Renaudin, J.-M. Nedelec, R. J. Wiglusz, Effect of lithium substitution on the charge compensation, structural and luminescence properties of nanocrystalline $Ca_{10}(PO_4)_6F_2$ activated with Eu^{3+} ions, CrystEngComm. 18 (2016) 3447-3455. DOI: 10.1039/C6CE00320F

[47] M. E. Fleet, Y. Pan, Site preference of rare earth elements in fluorapatite: Binary (LREE+HREE)–substituted crystals, Am. Mineral. 82 (1997) 870–877.

[48] M. E. Fleet, Y. Pan, Site preference of rare earth elements in fluorapatite, Am. Mineral. 80 (1995) 329–335.

[49] J. M. Hughes, M. Cameron, K. D. Crowley, Structural variations in natural F, OH, and Cl apatites Locality: Durango Mexico, Am. Mineral. 74 (1989) 870-876.

[50] D. S. Spencer, A. S. Puranik, N. A. Peppas, Intelligent nanoparticles for advanced drug delivery in cancer treatment, Curr. Opin. Chem. Eng. 7 (2015) 84–92. https://doi.org/10.1016/j.coche.2014.12.003

[51] K. T. Thurn, E. M. B. Brown, A. Wu, S. Vogt, B. Lai, J. Maser, T. Paunesku, G. E. Woloschak, Nanoparticles for Applications in Cellular Imaging, Nanoscale Res. Lett. 2 (2007) 430. DOI 10.1007/s11671-007-9081-5

[52] C. Leycuras, H. L. Gall, and J. M. Desvignes, Magneto-optic and magnetic properties of praseodymium substituted garnets, J. App. Phys. 53 (1982) 8181. https://doi.org/10.1063/1.330285

[53] J. Kong, Z. Liu, D. Cai, Y. Fan, P. Zhao, X. Liu, P. Pu, L. Song, C. He, A gadolinium-based magnetic resonance imaging contrast agent for nucleotides sensing, Sensor Actuat. B: Chem. 256 (2018) 913–920. https://doi.org/10.1016/j.snb.2017.10.026

Research highlights

- Pr^{3+} doped fluorapatite nanocrystals obtained by co-precipitation and calcination
- Luminescent Pr^{3+} doped fluorapatite nanocrystals have high biocompatibility
- The luminescence of Pr^{3+} doped fluorapatite nanocrystals has multicolor properties
- Multicolor properties and uptake allow intracellular tracking
- Nanocrystals entered the cancer cell models and are positioned in the cytoplasm.